

A Schwarzschild model of the Galactic bar with initial density from N-body simulations

Youngang Wang^{1*}, Shude Mao^{2,3}, Richard J. Long^{2,3}, Juntai Shen⁴

¹Key Laboratory of Optical Astronomy, National Astronomical Observatories, Chinese Academy of Sciences, Beijing 100012, China

²National Astronomical Observatories, Chinese Academy of Sciences, A20 Datun Road, Chaoyang District, Beijing 100012, China

³Jodrell Bank Centre for Astrophysics, Alan Turing Building, The University of Manchester, Manchester M13 9PL, UK

⁴Key Laboratory for Research in Galaxies and Cosmology, Shanghai Astronomical Observatory, Chinese Academy of Sciences, 80 Nandan Road, Shanghai 200030, China

Accepted . Received .

ABSTRACT

Using the potential from N-body simulations, we construct the Galactic bar models with the Schwarzschild method. By varying the pattern speed and the position angle of the bar, we find that the best-fit bar model has pattern speed $\Omega_p = 40 \text{ km s}^{-1} \text{ kpc}^{-1}$, and bar angle $\theta_{\text{bar}} = 45^\circ$. N-body simulations show that the best-fit model is stable for more than 1.5 Gyrs. Combined with the results in Wang et al. (2012), we find that the bar angle and/or the pattern speed are not well constrained by BRAVA data in our Schwarzschild models. The proper motions predicted from our model are slightly larger than those observed in four fields. In the future, more kinematic data from the ground and space-based observations will enable us to refine our model of the Milky Way bar.

Key words: Galaxy: bulge – Galaxies: kinematics and dynamics – galaxies: structure

1 INTRODUCTION

Perhaps two-thirds of spiral galaxies in the Universe are barred (e.g. Lee et al. 2012). Although there are several formation scenarios for the galactic bar (Athanasoula et al. 2013; Saha & Naab 2013), the issue is not yet completely settled. Both tidal interactions and internal secular processes have been proposed (e.g. Kormendy & Kennicutt 2004; Athanasoula 2012), although the latter may be the dominating mechanism (Li et al. 2009). The nearest bar is the one in our own Galaxy. Its age and formation history still remain somewhat uncertain, despite the large amount of photometric and kinematic data (see below). In this context, understanding the Galactic bar offers important clues for understanding other barred structures in the universe.

The first evidence for a bar in our Galaxy is from 21-cm observations (de Vaucouleurs 1964). Due to extinction in optical wavelengths, optical observation of the bar is difficult. Direct evidence for a bar at the Galactic center comes from near-infrared studies (Blitz & Spergel 1991). Microlensing events also favour the existence of a bar in the inner Galaxy (Paczynski et al. 1994; Evans 1994; Zhao et al. 1995). Modelling of the surface brightness in inner regions of the Milky Way from COBE infrared observations has shown that the angle between the major axis of the bar and the Sun-Galactic center line, θ_{bar} , is in the range of $13.4^\circ - 40^\circ$ (Zhao 1994, 1996; Zhao et al. 1996; Binney et al. 1997). Dehnen (2000) used the Hercules stream to put constraints on the bar an-

gle $10^\circ < \theta_{\text{bar}} < 70^\circ$ and the bar pattern speed $\Omega_p = 47.9 \pm 3.9 \text{ km s}^{-1} \text{ kpc}^{-1}$. Minchev et al. (2007) used the Oort constants as a constraint, and found that $\Omega_p = 48.4 \pm 1.0 \text{ km s}^{-1} \text{ kpc}^{-1}$ and $20^\circ < \theta_{\text{bar}} < 45^\circ$. Considering some low-velocity streams, in addition to the Hercules stream, Minchev et al. (2010) found $\Omega_p = 47.1 \pm 1.8 \text{ km s}^{-1} \text{ kpc}^{-1}$ and $30^\circ < \theta_{\text{bar}} < 45^\circ$. On the other hand, studies of star counts indicate that the bar angle is no more than 45° (Stanek et al. 1994; Mao & Paczyński 2002; Rattenbury et al. 2007). A most recent study by Cao et al. (2013) indicates $\theta_{\text{bar}} = 30^\circ$.

Confusingly, some star count observations extending to larger longitudes found a separate, flat long bar with an orientation of 43° (Benjamin et al. 2005; Cabrera-Lavers et al. 2007). This is also supported by a recent 6.7 GHz methanol maser investigation (45° , Green et al. 2011). A recent simulation suggested that both the inner bar and the long thin bar found by these studies may be manifestations of the same bar structure (Martinez-Valpuesta & Gerhard 2011).

A beneficial approach is to constrain the bar model by combining photometric data with kinematics. Using Schwarzschild’s orbit-superposition technique, Zhao (1996, hereafter ZH96) constructed a self-consistent bar model by using limited kinematic data. This model reproduced the observed surface brightness, velocity and velocity dispersion measurements in Baade’s Window. However, the radial velocity predicted from ZH96 is larger than that observed by the Bulge Radial Velocity Assay (BRAVA, Howard et al. 2008). The N-body models of Fux (1997, 1999), Sevenster et al. (1999)

* email: wangyg@bao.ac.cn

and other self-consistent models (Häfner et al. 2000; Bissantz et al. 2004) also used only limited kinematic data.

Taking into account observations of the inner regions of the Milky Way by the Hubble Space Telescope (e.g. Kozłowski et al. 2006; Clarkson et al. 2008; Soto et al. 2012), the Optical Gravitational Lensing Experiment (OGLE: Udalski et al. 2000; Sumi et al. 2004) and BRAVA (Rich et al. 2007; Howard et al. 2008; Kunder et al. 2012), extensive higher quality kinematic bar data are now available which can help improve bar modelling. Recently, Wang et al. (2012, hereafter Paper I) constructed a new self-consistent bar model using the orbit-superposition technique and utilising the BRAVA data. The density distribution in Paper I is similar to ZH96, the main differences being the bar angle and disk mass. The new model fits the radial velocity and velocity dispersion well in the BRAVA fields. However, the proper motions predicted from Paper I, along specific Galactic longitudes, are larger than those observed. One possible reason is that the density profile adopted in Paper I is invalid, or there may be contaminated by disc stars. The model density profile was obtained by modelling the surface brightness distribution from *low resolution* COBE observations.

The aim of this paper is to use an alternative density distribution to construct a self-consistent bar model. The density distribution adopted here is from the N-body model by Shen et al. (2010) (hereafter Shen10). Compared with the density model in Paper I, the Shen10 model has two advantages: (1) the model fits the BRAVA data well; (2) the model is simple. While the density distribution in Paper I has three components, a prolate bar, a boxy bulge and an axi-symmetric disk, the Shen10's model has only a bulge and a spherical dark matter halo.

There are two popular methods which can be used to construct the dynamical models. One is Schwarzschild's orbit-superposition technique (Schwarzschild 1979), which has been applied to external galaxies (e.g. Sambhus & Sridhar 2002; Cappellari et al. 2006; van den Bosch et al. 2008; Shen & Gebhardt 2010), and has also been used to construct self-consistent Galactic bar models (Zhao 1996; Häfner et al. 2000, and Paper I). The other is the Made-to-Measure (M2M) algorithm (Syer & Tremaine 1996; Jourdeuil & Emsellem 2007; de Lorenzi et al. 2007, 2008; Dehnen 2009; Long & Mao 2010; Das et al. 2011; Long & Mao 2012; Morganti & Gerhard 2012), which was applied to the Milky Way by Bissantz et al. (2004). However, only the equatorial surface brightness of the Milky Way was used in their model: no kinematic constraints were applied and their effective field is small. Most recently, in a companion paper, Long et al. (2013, hereafter Long13) improved the M2M modelling, by adapting it to a rotating frame. The density model used in Long13 is also from Shen10's simulation. The radial velocity and velocity dispersion predicted from the M2M model not only fit the BRAVA data, but also match Shen10's results. Therefore, another motivation of this paper is to compare the results from Schwarzschild's method with those from M2M. Throughout this paper, we adopt the velocity unit as km s^{-1} , and the distance unit as kpc. Correspondingly, the time unit in our paper is 0.98 Gyr.

2 MODEL AND POTENTIAL

In Shen10, the bar is evolved from an initially unbarred, thin disk. The disk mass is $M_d = 4.25 \times 10^{10} M_\odot$, which is realized by 10^6 equal mass particles. Around the disk, there is a rigid pseudo-isothermal halo with potential $\Phi = \frac{1}{2}v_c^2 \ln(1 + \frac{r^2}{R_c^2})$, where $V_c \approx$

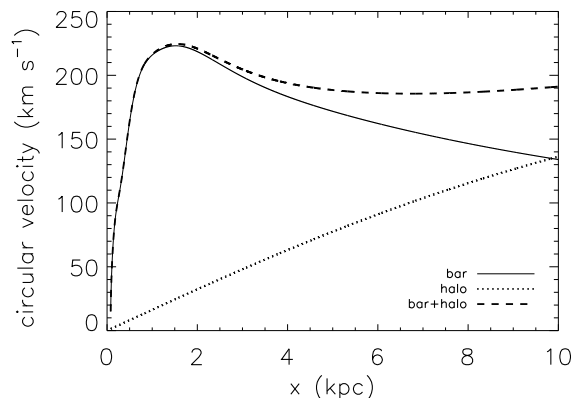


Figure 1. Circular velocity along the major axis of the bar. The solid, dotted and dashed lines represent the bar, halo, and bar+halo, respectively.

250 km s^{-1} , and $R_c \approx 15 \text{ kpc}$ is the core radius; these values are the same as those in Shen10. Regarding the rotation curve, although in Shen10 the initial rotation curve has $V_c \sim 200 - 220 \text{ km s}^{-1}$ between 5 to 20 kpc, after the bar forms the rotation curve at the solar position does change considerably to a lower value, same as shown in the present paper (Fig. 1). From the different snapshots in simulation, Shen10 obtained a bar pattern speed $\Omega_p = 40 \text{ km s}^{-1} \text{ kpc}^{-1}$.

In order to obtain the potential and the accelerations of the model particles for the disk, we follow the self-consistent field method of Hernquist & Ostriker (1992). The rotation curve of the model is shown in Figure 1 along the major axis of the bar. It can be seen that the circular velocity is nearly constant with a value of $v_{\text{circ}} \approx 190 \text{ km s}^{-1}$ beyond 4 kpc, which is slightly smaller than observations in several studies (Fich et al. 1989; Ghez et al. 2008; Reid et al. 2009; Bovy et al. 2012, see also Widrow et al. 2008 for theoretical models), but still consistent with those in Xue et al. (2008) and Sofue et al. (2009). The peak of the rotation curve in our model is at $\sim 1.5 \text{ kpc}$, while that in observations is at 0.3-0.5 kpc (Sofue et al. 2009). This difference likely originates from the initial conditions of the N-body simulation, where the bar is evolved from a thin exponential disk with scale length $\sim 1.9 \text{ kpc}$ and scale height 0.2 kpc.

3 KINEMATIC DATA

The kinematic data used in this paper are the radial velocities and velocity dispersions from four years of observations by the BRAVA project. The data are described in Howard et al. (2008) and Kunder et al. (2012). The data comprise 3 stripes along $b = -4^\circ, -6^\circ, -8^\circ$ together with some fields along the minor axis ($l = 0^\circ$).

4 MODEL CONSTRUCTION

4.1 Orbit-superposition technique

The key point of Schwarzschild's orbit superposition technique is to construct many orbits which can be used to reproduce the input model and other available observations. From the solutions of the linear equations, we can obtain the weight of each orbit. Combined

with the position and velocity in orbits, we can construct the full phase-space distribution function of the model.

The system of linear equations can be written as

$$\mu_i = \frac{\sum_{j=1}^{N_o} W_j O_{ij} V_{ij}}{\sum_{j=1}^{N_o} W_j O_{ij}}, \quad i = 1, \dots, N_c \quad (1)$$

where μ_i can be the volume density, surface density, the average moment, or higher order velocity moments in each cell i . N_o is the total number of orbits, N_c is the number of the spatial cells, O_{ij} is the time the orbits spends in each cell, V_{ij} are velocity, and high order velocity components in each cell. Following Paper I, we divide the first octant into 1000 cells. Due to the model symmetry, the other octants are reflected to the first octant. In each x -, y - and z - direction, the system is divided into 10 bins. The axis ratios of the bar in the inner 5 kpc are 1:0.8:0.4, so each cell is a box with $dx = 0.5$ kpc, $dy = 0.4$ kpc and $dz = 0.2$ kpc.

More practically, equation 1 can be written as a set of linear equations

$$\sum_{j=1}^{N_o} (\mu_i - V_{ij}) O_{ij} W_j = 0, \quad \text{for } i = 1, N_c \quad (2)$$

We adopt the non-negative least squares (NNLS) method (Pfenniger 1984) to solve for W_j by minimising χ_w^2 , where

$$\chi_w^2 = \sum_{i=1}^{N_c} \left| \sum_{j=1}^{N_o} (\mu_i - V_{ij}) O_{ij} W_j \right|^2. \quad (3)$$

The distribution of orbit weights for the solution with the smallest χ_w^2 may not be smooth, and thus artificial. Here we use two different smoothing methods. First, we require orbits with adjacent initial conditions to have nearly the same weight (Merritt & Fridman 1996). In this approach, Equation 3 becomes

$$\chi_w^2 = \sum_{i=1}^{N_c} \left| \sum_{j=1}^{N_o} (\mu_i - V_{ij}) O_{ij} W_j \right|^2 + \lambda \sum_{j=1}^{N_o} W_j^2 \quad (4)$$

where λ is a positive smoothing parameter and $\lambda = N_o^{-2}$. We vary the value of the smoothing parameter λ . However, our results are not sensitive to reasonable variations of λ . This is consistent with the findings in Shen & Gebhardt (2010). The second smoothing method we use is the same as that adopted in ZH96. The key point of this method is that orbits with similar integrals of motion have similar weights. We have compared the results from these two smoothing methods and found no significant difference between them (see also paper I). From now on, only results from the first smoothing method will be presented.

4.2 Initial conditions for orbits

The bar is known to be non-spherical with ‘figure rotation’ (e.g. Binney et al. 1997; Englmaier & Gerhard 1999; Debattista et al. 2002; Gerhard 2010). In such a system, only Jacobi’s energy is an integral of motion (Binney & Tremaine 2008). Therefore, it is not straightforward to construct a full phase-space density distribution. Fortunately, three methods have been shown to be effective in generating the initial conditions for orbits in this type of system. These methods are described in ZH96, Häfner et al. (2000) and Deibel et al. (2011). In Paper I, we compared the first two methods and found that there is no significant difference between them. Therefore, we follow Paper I and use ZH96’s method to construct

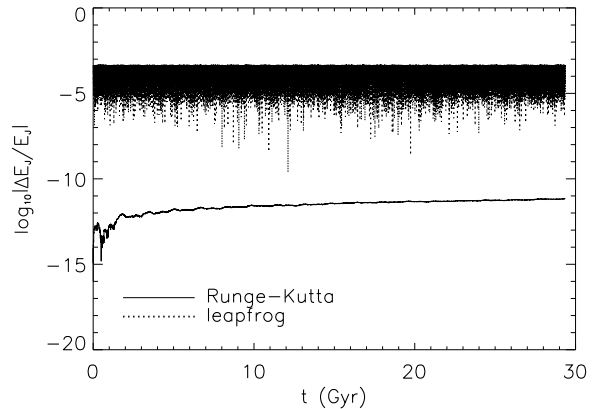


Figure 2. Fractional Jacobi’s energy deviation as a function of time for 7/8 order Runge-Kutta (solid line) and leapfrog integrator (dotted line).

the orbit library. Here we give a brief description of the main points of this method, and refer the reader to ZH96 for more details. The orbits are launched tangentially with a speed less than the circular velocity from a local apogalacticon. Moreover, orbits are launched in close pairs perpendicularly from the xz -, yz - or xy -symmetry plane, or from the x or y axis. If two orbits are launched perpendicularly from one plane, the close pairs will have opposite velocity.

We construct different models by varying the pattern speed, and for each model we generate ~ 13000 orbits.

4.3 Orbit integration

Popular integration methods for orbits include the modified Euler, leapfrog, Runge-Kutta and Hermite integrators. It has been shown that the fractional energy error is the smallest for the Runge-Kutta integrator if the integration time is short, while the leapfrog integrator is the best method if the integration time is long (Springel 2005; Binney & Tremaine 2008). We follow the method proposed by Quinn et al. (2010) to revise the general leap-frog integrator and make it appropriate to a system with figure rotation. We also improve the common 7/8 order Runge-Kutta algorithm, which can give an equal time output and keeps the Jacobi’s energy as a constant with high accuracy. Figure 2 shows the fractional Jacobi’s energy deviation as a function of time for both the 7/8 order Runge-Kutta and the leapfrog integrator. The integration time step Δt for the leapfrog method is 10^{-5} ($\approx 10^4$ years). Clearly, the 7/8 order Runge-Kutta integrator has higher accuracy (but with a very slow energy drift) than the leapfrog integrator even though the integration duration is over two Hubble times. Reducing Δt to 10^{-6} , the result remains similar. Therefore, we use the 7/8 order Runge-Kutta algorithm to carry out the orbit integrations. Every orbit is integrated for one Hubble time, which corresponds to ~ 200 dynamical times in the solar neighbourhood.

5 RESULTS

As shown in Paper I, the kinematics strongly depend on the pattern speed of the bar, and the projected density strongly depends on the bar angle. We calculate 30 models (see Table 1) by varying the model pattern speed and bar angle. As shown in Skokos et al. (2002), the strength of the bar is correlated with the pattern speed,

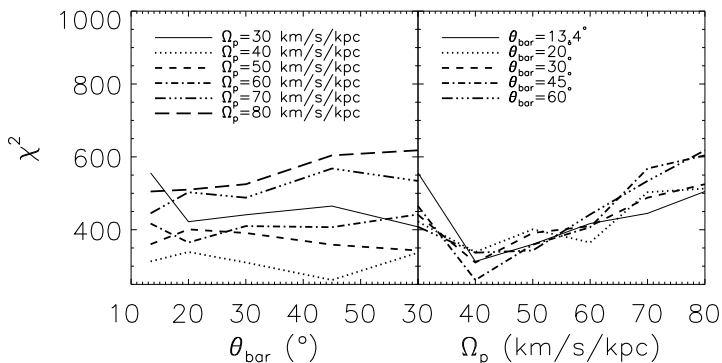


Figure 3. χ^2 distribution for different bar model. Left: Each line has the same pattern speed. Right: Each line has the same bar angle.

however, we have only one N-body simulation. Therefore, we vary the pattern speed but keep the density distribution of the bar fixed. This may be ‘artificial’ physically. In the context of this paper, however, it is a valid step to experiment (keeping the density fixed). In each model, we run the orbit-superposition technique to test the self-consistency. The volume density, projected density, radial velocity and velocity dispersion in four stripes $b = -4^\circ$, $b = -6^\circ$, $b = -8^\circ$ and $l = 0^\circ$ (see Figure 6) are used as constraints to produce the weight of each orbit. The volume and projected densities are derived directly from the N-body density distribution of the bar. For volume density, only the inner 5 kpc are considered because our aim is to check the self-consistency of the bar. The radial velocity and velocity dispersion are from the BRAVA survey (Howard et al. 2008; Kunder et al. 2012). The projected density, the radial velocity and velocity dispersion are fitted in the range $l = [-12^\circ, 12^\circ]$, $b = [-10^\circ, 10^\circ]$. As described in section 4.1, the orbit weights in Equation 1 are determined by the NNLS method and are smoothed by following Merritt & Fridman (1996) and Paper I.

A self-consistent model should reconstruct the input volume density and projected density well. All our models satisfy these requirements. In order to select the best model, we calculate the χ^2 value between the observed and reconstructed radial velocity and velocity dispersion for each model. χ^2 is defined as

$$\chi^2 = \sum_{i=1}^{N_{\text{obs}}} \frac{(y_{\text{obs}} - y_{\text{model}})^2}{\sigma_{\text{obs}}^2}, \quad (5)$$

where N_{obs} is the total number of observed data points, y_{obs} and y_{model} are the observed and model predicted kinematics, respectively. In Table 1, we show the values of χ^2 for our 30 models. It is clear that the best-fit model is Model 9. Figure 3 shows the results graphically. The left panel shows the bar angle is ill constrained while the bar pattern speed is better determined at $\Omega_p = 40 \text{ km s}^{-1} \text{ kpc}^{-1}$. The trends are not dissimilar to Figure 4 in Long et al. (2013), showing that Schwarzschild and M2M methods are, as expected, in agreement with each other.

In Figures 4 and 5, we show the volume density and projected density contours, respectively, for Model 9. In each figure, the solid and dotted lines represent the input data and models. Clearly, Model 9 can reproduce the volume density and projected density distributions well in most bar regions. The deviation between the input projected density and the reconstructed one is below 5% in the inner bar region. For the volume density, the reconstruction is not so good

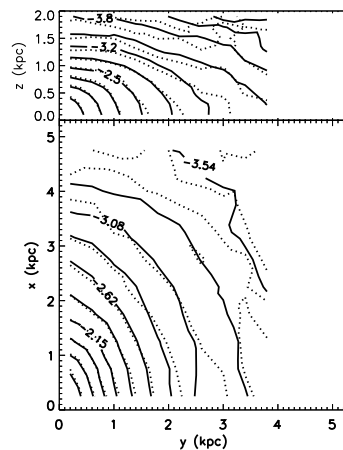


Figure 4. Volume density contours from the input model (solid lines) and from orbits (dotted lines) in the $x - y$ (bottom panel) and $y - z$ (top panel) planes for Model 9.

in the outer part. One reason is that our input model is an N-body model, the number of particles in the outer region is low. Notice that the surface density map in Fig. 5 does not show a pronounced asymmetry as the corresponding surface brightness map (see Fig. 1 in Shen10) since the latter accounts for the distance effect which amplifies the asymmetry.

The middle panel of Figure 6 shows the velocity and velocity dispersion distribution for the best-fit model, Model 9. It is seen that Model 9 can fit the BRAVA data well except a few points. The results for Model 4 ($\Omega_p = 30 \text{ km s}^{-1} \text{ kpc}^{-1}$, $\theta_{\text{bar}} = 45^\circ$) and Model 29 ($\Omega_p = 80 \text{ km s}^{-1} \text{ kpc}^{-1}$, $\theta_{\text{bar}} = 45^\circ$) are also given for comparison. Some wiggles in the reconstructed kinematic profiles are clearly seen. There are two reasons for this: (1) our input model is from an N-body simulation, the phase space distribution is not smooth. Note that the velocity profiles in Shen et al. (2010) are smoother than those presented here, because they used $2^\circ \times 2^\circ$ bins while we use $1^\circ \times 1^\circ$ bins. (2) In order to reconstruct the phase space distribution of the Galactic bar, we did not add any more constraints during the model fit. Therefore, regions without data may have wiggles.

The proper motions in four fields, from observations and from the model, for Model 9 are also given in Table 2. It can be seen that the model proper motions along the longitudinal direction are slightly larger than those observed. Comparing with the proper motions predicted in Paper I, the proper motions predicted here are smaller, which indicates that we have reduced the discrepancy between the model predictions and observations. In order to make further comparisons of the proper motions from our model with observations, we need additional data. The predicted proper motions of Model 9 in the range $l = [-12^\circ, 12^\circ]$, $b = [-10^\circ, 10^\circ]$ are available online¹.

Stability is one of the important properties for an ‘optimal’ dynamical model. We follow the method described in Paper I to check the stability of Model 9. Figure 7 shows the evolution of $-2K/W$ and three moments of inertial I_{xx} (where x is defined along the initial major axis), I_{zz} (along the initial minor axis) and I_{xy} (cross term) of the bar, where W is the Claussius Virial of the system and K is the total kinetic energy. One can see that $W + 2K$

¹ <http://cosmology.bao.ac.cn/~wangy/>

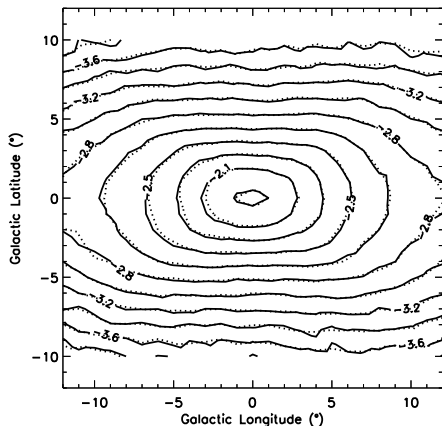


Figure 5. Projected surface density contours from the input model (solid lines) and from orbits (dotted lines) for Model 9.

satisfies the Virial theorem well. Moreover, the cross term I_{xy} in the rest frame follows nearly a sinusoidal curve with a constant period 0.08 Gyr, which is in good agreement with half period of bar’s rotation presented $\pi/\Omega_p \sim 0.08$ Gyr. Therefore, our bar model is stable at least within 1.5 Gyrs, which is more stable than the previous bar model in Paper I. Incidentally, this is slightly longer than the stable period shown in other studies (e.g., Zhao 1996).

6 SUMMARY AND DISCUSSION

Based on the N -body simulation in Shen10, we have constructed 30 bar models with different pattern speeds and bar angles using Schwarzschild’s method. The χ^2 values show that the best model has $\Omega_p = 40 \text{ km s}^{-1} \text{ kpc}^{-1}$ and bar angle $\theta_{\text{bar}} = 45^\circ$. The pattern speed is in good agreement with those obtained from Shen’s numerical simulation and the M2M method, while the bar angle is different from but still consistent with that obtained from the M2M method ($\theta_{\text{bar}} = 30^\circ$, Long13), since the bar angle is weakly constrained, as found in the N -body simulation and M2M. We have fitted the galactic-centric radial velocity from the BRAVA survey with our models. However, the BRAVA survey adopts a rotation velocity of $v_{\text{circ}} \approx 220 \text{ km s}^{-1}$ in the solar neighbourhood (Howard et al. 2008), which differs from 190 km s^{-1} at 8 kpc in our simulation. Since the projection of the solar circular motion along the line of sight is $v_{\text{circ}} \cos b \sin l$, the difference in the rotation velocity will cause a systematic offset. However, even at our largest longitude $|l| = 10^\circ$ (and $b = 0^\circ$), this will only introduce a systematic offset of 5.2 km s^{-1} , comparable to the error bar in our average velocity ($5 - 10 \text{ km s}^{-1}$), and so we do not expect this difference will change our results significantly. The best-fit model can reconstruct the volume and projected densities of the numerical bar well, and can also fit the observed radial velocities and velocity dispersions in the BRAVA fields. The proper motions, along specific Galactic longitudes, predicted by our model are slightly larger than those in observations. Compared to the model in Paper I, our best-fit model has better agreement of the proper motions along the Galactic longitude with observations than Paper I. Moreover, the stability of the bar in Model 9 is better than that in Paper I. From the studies here and Paper I, we draw some conclusions:

(i) The BRAVA data can be fitted by models within large parameter ranges - the pattern speed can be from $\Omega_p = 40 \text{ km s}^{-1} \text{ kpc}^{-1}$

to $\Omega_p = 80 \text{ km s}^{-1} \text{ kpc}^{-1}$, and the bar angle from $\theta_{\text{bar}} = 13.4^\circ$ to $\theta_{\text{bar}} = 60^\circ$. In other words, it is not easy to say which model is the best-fit model from the BRAVA data alone. Moreover, it seems that there is a degeneracy between the pattern speed and the density distribution of the model. In paper I, $\Omega_p = 60 \text{ km s}^{-1} \text{ kpc}^{-1}$ can fit the data well, while $\Omega_p = 40 \text{ km s}^{-1} \text{ kpc}^{-1}$ can best fit the data here.

(ii) Observed proper motions can help us to reduce the model degeneracy. A comparison indicates that the best fit with the observed data is $\Omega_p = 40 \text{ km s}^{-1} \text{ kpc}^{-1}$. However, the proper motions along Galactic longitudes predicted by our model are slightly larger than those in observations. One possible reason is that the density model adopted is not yet sufficiently representative of the Milky Way. At present, most density models of the bar are constructed by using only the surface brightness, star counts, or from N -body simulations. We need to construct the density distribution of the bar model by combining all of them, especially if the proper motion constraints are to be matched. Another possible reason is that the proper motion data in the bar may be contaminated by disk stars. We also note that proper motions of the same field from different observations give somewhat discrepant values (e.g., see Table 2 for values for Baade’s window).

Clearly more proper motion data are desirable. It will also be important to consider other probes of kinematics, such as those considered by Dehnen (2000, for more recent data, see Liu et al. 2012) to constrain bar parameters. Future data from APOGEE (Eisenstein et al. 2011) and ARGOS (Freeman et al. 2013) will provide new chemo-dynamical constraints on the Galactic bar, which will challenge all current modelling methods and provide strong clues about how did the bar in our Galaxy form.

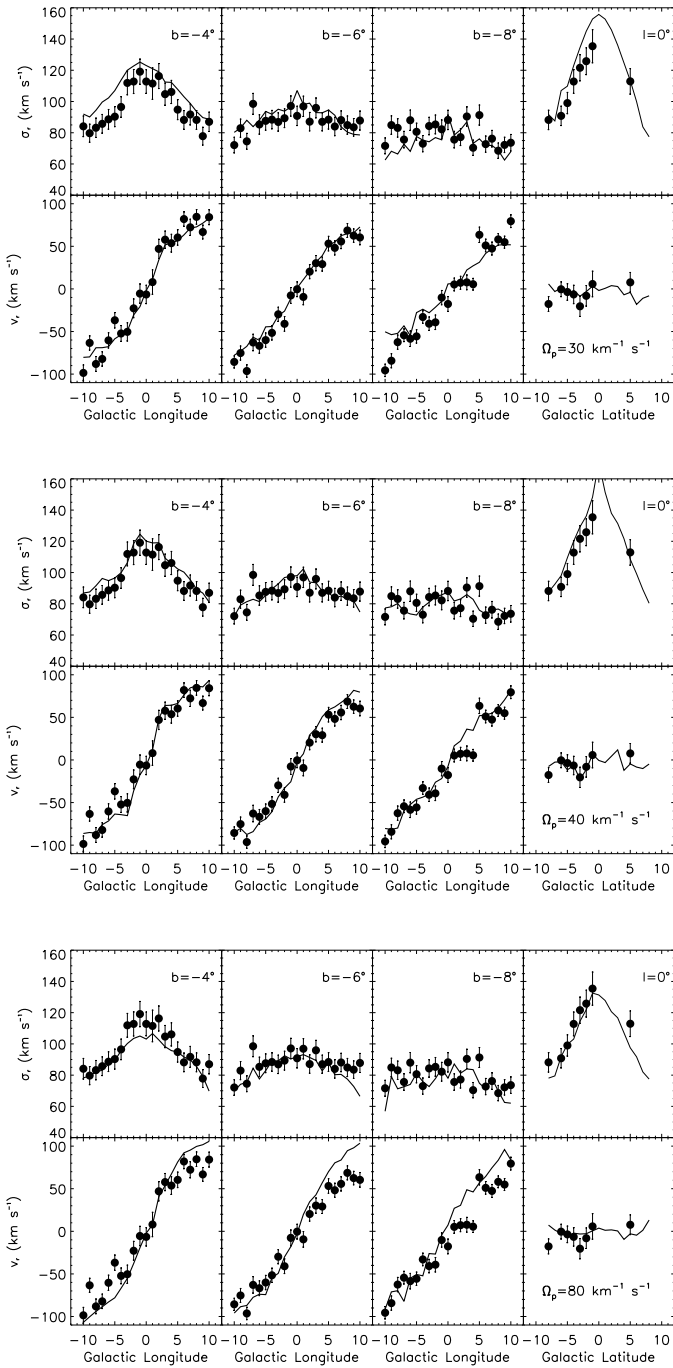


Figure 6. Radial velocity and velocity dispersion distributions for Model 4 (top panel: $\Omega_p = 30 \text{ km s}^{-1} \text{ kpc}^{-1}$, $\theta_{\text{bar}} = 45^\circ$), Model 9 (middle panel: $\Omega_p = 40 \text{ km s}^{-1} \text{ kpc}^{-1}$, $\theta_{\text{bar}} = 45^\circ$) and Model 29 (bottom panel: $\Omega_p = 80 \text{ km s}^{-1} \text{ kpc}^{-1}$, $\theta_{\text{bar}} = 45^\circ$). The solid line is for the model while the filled circles represent data from BRAVA.

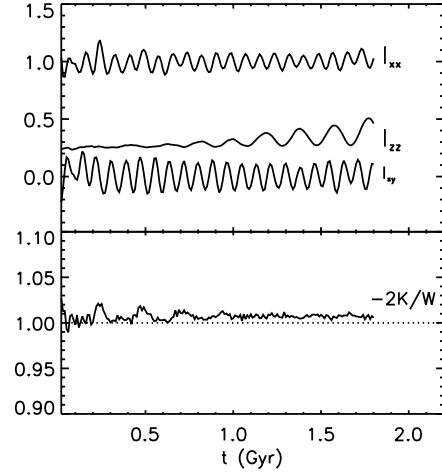


Figure 7. Evolution of $-2K/W$ (lower panel) and the three moments of inertia I_{xx} , I_{zz} and I_{xy} for our best-fit Model 9. All the quantities plotted here are calculated in the inertial frame, where the x axis is aligned with the initial major axis of the bar.

Table 1. χ^2 from fitting the velocity and velocity dispersion of BRAVA data for different input models.

Model ID	Ω_p ($\text{km s}^{-1} \text{kpc}^{-1}$)	θ_{bar} ($^\circ$)	χ^2
1	30	13.4	556
2	30	20	422
3	30	30	441
4	30	45	465
5	30	60	408
6	40	13.4	313
7	40	20	339
8	40	30	310
9	40	45	262
10	40	60	337
11	50	13.4	360
12	50	20	401
13	50	30	391
14	50	45	359
15	50	60	343
16	60	13.4	417
17	60	20	365
18	60	30	410
19	60	45	407
20	60	60	442
21	70	13.4	445
22	70	20	503
23	70	30	488
24	70	45	568
25	70	60	534
26	80	13.4	505
27	80	20	510
28	80	30	525
29	80	45	604
30	80	60	618

Table 2. Observed and predicted proper motion dispersions in some fields, the bottom four rows are predictions from Paper I.

Field	(l,b)	σ_l	σ_b	Ref.
	($^\circ$)	(mas yr $^{-1}$)	(mas yr $^{-1}$)	
Baade's Window	(1,-4)	3.2 ± 0.1	2.8 ± 0.1	Spaenhauer et al. (1992)
Baade's Window	(1,-4)	3.14 ± 0.11	2.74 ± 0.08	Zhao et al. (1996)
Baade's Window	(1.13,-3.77)	2.9	2.5	Kuijken & Rich (2002)
Baade's Window	(1,-4)	2.87 ± 0.08	2.59 ± 0.08	Kozłowski et al. (2006)
Baade's Window	(0.9,-4)	3.06 ± 0.11	2.79 ± 0.13	Soto et al. (2007)
Baade's Window	(1,-4)	3.13 ± 0.16	2.50 ± 0.10	Babusiaux et al. (2010)
Baade's Window	(1.13,-3.76)	3.08 ± 0.08	2.74 ± 0.13	Soto et al. (2012)
Plaut's Window	(0,-8)	3.39 ± 0.11	2.91 ± 0.09	Vieira et al. (2007, 2009)
Sagittarius I	(1.25,-2.65)	3.3	2.7	Kuijken & Rich (2002)
Sagittarius I	(1.27,-2.66)	3.07 ± 0.08	2.73 ± 0.07	Kozłowski et al. (2006)
Sagittarius I	(1.25,-2.65)	3.067	2.760	Clarkson et al. (2008)
Sagittarius I	(1.26,-2.65)	3.11 ± 0.08	2.71 ± 0.08	Soto et al. (2012)
NGC 6558	(0.28,-6.17)	2.45 ± 0.11	2.37 ± 0.13	Soto et al. (2012)
Baade's Window	(1,-4)	3.74	2.49	Model 9
Plaut's Window	(0,-8)	3.43	2.40	Model 9
Sagittarius I	(1,-3)	3.61	2.58	Model 9
NGC 6558	(0,-6)	3.67	2.48	Model 9
Baade's Window	(1,-4)	4.44	2.52	Wang et al. (2012)
Plaut's Window	(0,-8)	5.28	2.32	Wang et al. (2012)
Sagittarius I	(1,-3)	4.43	2.67	Wang et al. (2012)
NGC 6558	(0,-6)	4.46	2.36	Wang et al. (2012)

ACKNOWLEDGMENTS

We thank the referee for comments and suggestions that improved the paper. We acknowledge helpful discussions with Simon White. We also thank Jie Wang and Bin Yue, who helped us to revise the Gadget code and run N-body simulations. This work was started during the 2011 workshop on the Galactic bulge and bar in the Aspen Center for Physics. We thank the hospitality of the Aspen Center for Physics, which is supported by the NSF grant 1066293. YGW acknowledges the support by the National Science Foundation of China (Grant No. Y011061001 and No. Y122071001). SM and RJL acknowledge the financial support of the Chinese Academy of Sciences and NAOC. JS acknowledges the support by the National Science Foundation of China (Grant no. 11073037) and by the 973 Program of China (Grant no. 2009CB824800). Computer runs were performed on the *Laohu* computer cluster of NAOC and the Supercomputing Center of Chinese Academy of Sciences.

REFERENCES

Athanassoula E., 2012, ArXiv e-prints
 Athanassoula E., Machado R. E. G., Rodionov S. A., 2013, MNRAS, 429, 1949
 Babusiaux C., Gómez A., Hill V., Royer F., Zoccali M., Arenou F., Fux R., Lecureur A., Schultheis M., Barbuy B., Minniti D., Ortolani S., 2010, A&A, 519, A77
 Benjamin R. A., Churchwell E., Babler B. L., Indebetouw e. a., 2005, ApJ, 630, L149
 Binney J., Gerhard O., Spergel D., 1997, MNRAS, 288, 365
 Binney J., Tremaine S., 2008, Galactic Dynamics: Second Edition. Princeton University Press
 Bissantz N., Debattista V. P., Gerhard O., 2004, ApJ, 601, L155
 Blitz L., Spergel D. N., 1991, ApJ, 379, 631
 Bovy J., Allende Prieto C., Beers T. C., Bizyaev D., da Costa L. N., Cunha K., Ebelke G. L., Eisenstein D. J., Frinchaboy P. M., García Pérez A. E., Girardi L., Hearty F. R., Hogg D. W., Holtzman J., Maia M. A. G., Majewski S. R., Malanushenko E., Malanushenko V., Mészáros S., Nidever D. L., O’Connell R. W., O’Donnell C., Oravetz A., Pan K., Rocha-Pinto H. J., Schiavon R. P., Schneider D. P., Schultheis M., Skrutskie M., Smith V. V., Weinberg D. H., Wilson J. C., Zasowski G., 2012, ApJ, 759, 131
 Cabrera-Lavers A., Hammersley P. L., González-Fernández C., López-Corredoira M., Garzón F., Mahoney T. J., 2007, A&A, 465, 825
 Cao L., Mao S., Nataf D., Rattenbury N. J., Gould A., 2013, ArXiv e-prints
 Cappellari M., Bacon R., Bureau M., Damen M. C., Davies R. L., de Zeeuw P. T., Emsellem E., Falcón-Barroso J., Krajnović D., Kuntschner H., McDermid R. M., Peletier R. F., Sarzi M., van den Bosch R. C. E., van de Ven G., 2006, MNRAS, 366, 1126
 Clarkson W., Sahu K., Anderson J., Smith T. E., Brown T. M., Rich R. M., Casertano S., Bond H. E., Livio M., Minniti D., Panagia N., Renzini A., Valenti J., Zoccali M., 2008, ApJ, 684, 1110
 Das P., Gerhard O., Mendez R. H., Teodorescu A. M., de Lorenzi F., 2011, MNRAS, 415, 1244
 de Lorenzi F., Debattista V. P., Gerhard O., Sambhus N., 2007, MNRAS, 376, 71
 de Lorenzi F., Gerhard O., Saglia R. P., Sambhus N., Debattista V. P., Pannella M., Méndez R. H., 2008, MNRAS, 385, 1729

de Vaucouleurs G., 1964, in F. J. Kerr ed., The Galaxy and the Magellanic Clouds Vol. 20 of IAU Symposium, Interpretation of velocity distribution of the inner regions of the Galaxy. p. 195
 Debattista V. P., Gerhard O., Sevenster M. N., 2002, MNRAS, 334, 355
 Dehnen W., 2000, AJ, 119, 800
 Dehnen W., 2009, MNRAS, 395, 1079
 Deibel A. T., Valluri M., Merritt D., 2011, ApJ, 728, 128
 Eisenstein D. J., Weinberg D. H., Agol E., Aihara H., Allende Prieto C., Anderson S. F., Arns J. A., Aubourg É., Bailey S., Balbinot E., et al. 2011, AJ, 142, 72
 Englmaier P., Gerhard O., 1999, MNRAS, 304, 512
 Evans N. W., 1994, ApJ, 437, L31
 Fich M., Blitz L., Stark A. A., 1989, ApJ, 342, 272
 Freeman K., Ness M., Wylie-de-Boer E., Athanassoula E., Bland-Hawthorn J., Asplund M., Lewis G., Yong D., Lane R., Kiss L., Ibata R., 2013, MNRAS, 428, 3660
 Fux R., 1997, A&A, 327, 983
 Fux R., 1999, A&A, 345, 787
 Gerhard O., 2010, ArXiv e-prints
 Ghez A. M., Salim S., Weinberg N. N., Lu J. R., Do T., Dunn J. K., Matthews K., Morris M. R., Yelda S., Becklin E. E., Kremenek T., Milosavljevic M., Naiman J., 2008, ApJ, 689, 1044
 Green J. A., Caswell J. L., McClure-Griffiths N. M., Avison A., Breen S. L., Burton M. G., Ellingsen S. P., Fuller G. A., Gray M. D., Pestalozzi M., Thompson M. A., Voronkov M. A., 2011, ArXiv e-prints
 Häfner R., Evans N. W., Dehnen W., Binney J., 2000, MNRAS, 314, 433
 Hernquist L., Ostriker J. P., 1992, ApJ, 386, 375
 Howard C. D., Rich R. M., Reitzel D. B., Koch A., De Propriis R., Zhao H., 2008, ApJ, 688, 1060
 Jourdeuil E., Emsellem E., 2007, in M. Kissler-Patig, J. R. Walsh, & M. M. Roth ed., Science Perspectives for 3D Spectroscopy Scalable N-body Code for the Modeling of Early-type Galaxies. p. 99
 Kormendy J., Kennicutt Jr. R. C., 2004, ARA&A, 42, 603
 Kozłowski S., Woźniak P. R., Mao S., Smith M. C., Sumi T., Vestrand W. T., Wyrzykowski Ł., 2006, MNRAS, 370, 435
 Kuijken K., Rich R. M., 2002, AJ, 124, 2054
 Kunder A., Koch A., Rich R. M., de Propriis R., Howard C. D., Stubbs S. A., Johnson C. I., Shen J., Wang Y., Robin A. C., Kormendy J., Soto M., Frinchaboy P., Reitzel D. B., Zhao H., Origlia L., 2012, AJ, 143, 57
 Lee G.-H., Park C., Lee M. G., Choi Y.-Y., 2012, ApJ, 745, 125
 Li C., Gadotti D. A., Mao S., Kauffmann G., 2009, MNRAS, 397, 726
 Liu C., Xue X., Fang M., van de Ven G., Wu Y., Smith M. C., Carrell K., 2012, ApJ, 753, L24
 Long R. J., Mao S., 2010, MNRAS, 405, 301
 Long R. J., Mao S., 2012, MNRAS, p. 2408
 Long R. J., Mao S., Shen J., Wang Y., 2013, MNRAS, 428, 3478
 Mao S., Paczyński B., 2002, MNRAS, 337, 895
 Martínez-Valpuesta I., Gerhard O., 2011, ApJ, 734, L20
 Merritt D., Fridman T., 1996, ApJ, 460, 136
 Minchev I., Boily C., Siebert A., Bienayme O., 2010, MNRAS, 407, 2122
 Minchev I., Nordhaus J., Quillen A. C., 2007, ApJ, 664, L31
 Morganti L., Gerhard O., 2012, MNRAS, p. 2607
 Paczynski B., Stanek K. Z., Udalski A., Szymanski M., Kaluzny J., Kubiak M., Mateo M., Krzemiński W., 1994, ApJ, 435, L113
 Pfenniger D., 1984, A&A, 141, 171

- Quinn T., Perrine R. P., Richardson D. C., Barnes R., 2010, *AJ*, 139, 803
- Rattenbury N. J., Mao S., Sumi T., Smith M. C., 2007, *MNRAS*, 378, 1064
- Reid M. J., Menten K. M., Zheng X. W., Brunthaler A., Moscadelli L., Xu Y., Zhang B., Sato M., Honma M., Hirota T., Hachisuka K., Choi Y. K., Moellenbrock G. A., Bartkiewicz A., 2009, *ApJ*, 700, 137
- Rich R. M., Reitzel D. B., Howard C. D., Zhao H., 2007, *ApJ*, 658, L29
- Saha K., Naab T., 2013, *ArXiv e-prints*
- Sambhus N., Sridhar S., 2002, *A&A*, 388, 766
- Schwarzschild M., 1979, *ApJ*, 232, 236
- Sevenster M., Saha P., Valls-Gabaud D., Fux R., 1999, *MNRAS*, 307, 584
- Shen J., Gebhardt K., 2010, *ApJ*, 711, 484
- Shen J., Rich R. M., Kormendy J., Howard C. D., De Propriis R., Kunder A., 2010, *ApJ*, 720, L72
- Skokos C., Patsis P. A., Athanassoula E., 2002, *MNRAS*, 333, 861
- Sofue Y., Honma M., Omodaka T., 2009, *PASJ*, 61, 227
- Soto M., Kuijken K., Rich R. M., 2012, *A&A*, 540, A48
- Soto M., Rich R. M., Kuijken K., 2007, *ApJ*, 665, L31
- Spaenhauer A., Jones B. F., Whitford A. E., 1992, *AJ*, 103, 297
- Springel V., 2005, *MNRAS*, 364, 1105
- Stanek K. Z., Mateo M., Udalski A., Szymanski M., Kaluzny J., Kubiak M., 1994, *ApJ*, 429, L73
- Sumi T., Wu X., Udalski A., Szymański M., Kubiak M., Pietrzyński G., Soszyński I., Woźniak P., Żebruń K., Szweczyk O., Wyrzykowski Ł., 2004, *MNRAS*, 348, 1439
- Syer D., Tremaine S., 1996, *MNRAS*, 282, 223
- Udalski A., Zebrun K., Szymanski M., Kubiak M., Pietrzynski G., Soszynski I., Wozniak P., 2000, *Acta Astron*, 50, 1
- van den Bosch R. C. E., van de Ven G., Verolme E. K., Cappellari M., de Zeeuw P. T., 2008, *MNRAS*, 385, 647
- Vieira K., Casetti-Dinescu D. I., Méndez R. A., Rich R. M., Girard T. M., Korchagin V. I., van Altena W., Majewski S. R., van den Bergh S., 2007, *AJ*, 134, 1432
- Vieira K., Casetti-Dinescu D. I., Méndez R. A., Rich R. M., Girard T. M., Korchagin V. I., van Altena W. F., Majeski S. R., van den Bergh S., 2009, in *Revista Mexicana de Astronomia y Astrofisica Conference Series Vol. 35 of Revista Mexicana de Astronomia y Astrofisica Conference Series, Proper Motions in the Galactic Bulge: Plaut's Window*. pp 123–124
- Widrow L. M., Pym B., Dubinski J., 2008, *ApJ*, 679, 1239
- Xue X. X., Rix H. W., Zhao G., Re Fiorentin P., Naab T., Steinmetz M., van den Bosch F. C., Beers T. C., Lee Y. S., Bell E. F., Rockosi C., Yanny B., Newberg H., Wilhelm R., Kang X., Smith M. C., Schneider D. P., 2008, *ApJ*, 684, 1143
- Wang Y., Zhao H., Mao S., Rich R. M., 2012, *MNRAS*, 427, 1429
- Zhao H., 1994, PhD thesis, Columbia Univ.
- Zhao H., Rich R. M., Biello J., 1996, *ApJ*, 470, 506
- Zhao H., Rich R. M., Spergel D. N., 1996, *MNRAS*, 282, 175
- Zhao H., Spergel D. N., Rich R. M., 1995, *ApJ*, 440, L13
- Zhao H. S., 1996, *MNRAS*, 283, 149